NASA

Technical Memorandum 82116

TRANSPORT OF INFRARED RADIATION IN CUBOIDAL CLOUDS

(NASA-TM-82116) TRANSPORT OF INFRARED RADIATION IN CUBOIDAL CLOUDS (NASA) 49 p
HC A03/MF A01 CSCL 04A
N81-25602
Unclas
G3/46 26051

Harshvardhan
James A. Weinman
Roger Davies

APRIL 1981

National Aeronautics and
Space Administration

Goddard Space Flight Center
Greenbelt, Maryland 20771

TRANSPORT OF INFRARED RADIATION IN CUBOIDAL CLOUDS

Harshvardhan[1,2]
James A. Weinman[2,3]
Roger Davies[3,4]

April 1981

---

[1] Dept. of Meteorology, Univ. of Maryland, College Park, MD 20742.
[2] Laboratory for Atmospheric Sciences, Goddard Space Flight Center, Greenbelt, MD 20771.
[3] Space Science and Engineering Center, Univ. of Wisconsin, Madison, WI 53706.
[4] Present affiliation: Dept. of Geosciences, Purdue University, West Lafayette, IN 47907.

GODDARD SPACE FLIGHT CENTER
Greenbelt, Maryland

TABLE OF CONTENTS

TRANSPORT OF INFRARED RADIATION IN CUBOIDAL CLOUDS

Harshvardhan
James A. Weinman
Roger Davies

ABSTRACT

The transport of infrared radiation in a single cuboidal cloud has been modeled using a vertical two-stream approximation. Computations have been made at 10μm for a Deirmendjian (1969) C-1 water cloud of single scattering albedo, $\tilde{\omega} = 0.638$ and asymmetry parameter, $g = 0.865$. Results indicate that the emittance of the top face of the model cloud is always less than that for a plane parallel cloud of the same optical depth. The hemispheric flux escaping from the cloud top has a gradient from the center to the edges which brighten when the cloud is over warmer ground. Cooling rate calculations in the 8–13.6μm region show that there is cooling out of the sides of the cloud at all levels even when there is heating of the core from the ground below.

The radiances exiting from model cuboidal clouds were computed by path integration over the source function obtained with the two-stream approximation. Results suggest that the brightness temperature measured from finite clouds will overestimate the cloud top temperature.

Some key results of the model have been compared with Monte Carlo simulations. Overall errors in flux and radiance average a few degrees for most cases.

TRANSPORT OF INFRARED RADIATION IN CUBOIDAL CLOUDS

1. INTRODUCTION

The role of clouds in determining the radiation field in general circulation and climate models has been widely considered. It has also been realized that the finite horizontal dimensions of individual clouds in convective cloud fields cannot be treated in the same manner as plane parallel clouds. The scattering of visible radiation by finite clouds has been studied by McKee and Cox (1974) and others, primarily using Monte Carlo methods, and by Davies and Weinman (1977), Barkstrom and Arduini (1977) and Davies (1978) who developed analytical solutions to this problem. Microwave radiances from finite rain clouds were computed by Weinman and Davies (1978) using an analytical method that was compared with Monte Carlo results. The question of infrared radiances from finite clouds has been addressed only recently by Liou and Ou (1979) and Ellingson and Kolczynski (1980); however, a number of considerations still require attention.

The purpose of this paper is to establish a simple analytical method that can be used to compute infrared radiation quantities in isolated finite clouds of cuboidal shape. This will be accomplished by comparing some key results with Monte Carlo computations. The analytical technique is such that allowances for vertical temperature variations can be made and in the future, the isolated model cloud may be embedded in a participating atmosphere. We have also not considered the effect of neighboring clouds.

2. VERTICAL TWO-STREAM APPROXIMATION

The equation of transfer in three dimensions cannot be solved analytically for arbitrary scattering. Various approximations to the equation and boundary conditions have therefore been suggested and utilized to obtain results for particular problems. Two recent applications in atmospheric radiative transfer are those of Davies (1978) who used the Delta-Eddington approximation in the visible and Liou and Ou (1979) who used the Eddington approximation in the infrared. Weinman and Davies (1978) have also computed microwave radiances emerging from rain clouds using the Eddington approximation. A problem with the Eddington approximation is that it can yield unrealistic results such as negative reflectance and values of emittance exceeding unity for certain ranges of the single scattering albedo, $\tilde{\omega}$, and asymmetry parameter, g. Lyzenga (1973) has shown that for a semi-infinite plane parallel layer, negative values of the diffuse reflectance are obtained in the Eddington approximation when

$$g > \frac{1}{3\tilde{\omega}} (4\tilde{\omega} - 1) \tag{1}$$

Unfortunately the range of parameters typical of clouds satisfies the above inequality because $g \sim 0.7$ to 0.8 and $\tilde{\omega} \sim 0.3$ to 0.6 in the infrared; hence, the Eddington approximation is inappropriate.

The two-stream approximation avoids the pitfall that Liou and Ou (1979) encountered, yet it yields similar governing equations. Recognizing that stratification within a horizontally finite cloud element would still be in the vertical direction, it is possible to introduce a vertical two-stream approximation to the three dimensional radiative transfer problem. The equation of transfer in three dimensions for a homogeneous cloud may be written in terms of the radiance, I, as

$$\nu \cos\phi \frac{\partial I}{\partial x} + \nu \sin\phi \frac{\partial I}{\partial y} + \mu \frac{\partial I}{\partial z} = - I + (1 - \tilde{\omega}) B + J_s \tag{2}$$

The horizontal and vertical axes are designated x, y and z, where z increases in the upward direction (see Fig. 1). The independent variables are in dimensionless optical thickness, τ, with the extinction coefficient, k, absorbed into the L.H.S. of the equation. The azimuth and zenith angles, ϕ and θ, where $\mu = \cos\theta$ and $\nu = \sin\theta$, are measured with respect to the x and z axes, respectively. The scattering source function is

$$J_s\,(x, y, z, \mu, \phi) = \frac{\tilde{\omega}}{4\pi} \int_0^{2\pi} \int_{-1}^{1} p\,(\mu, \phi; \mu', \phi')\, I\,(\mu', \phi')\, d\mu'\, d\phi' \qquad (3)$$

$\tilde{\omega}$ is the albedo for single scattering, $p\,(\mu, \phi; \mu', \phi')$ is the phase function for scattering from direction μ', ϕ' into μ, ϕ. The Planck function B may be linearized about its value at the top of the cloud, such that

$$B = B_0 + \beta z \qquad (4)$$

where β is a constant. However, for the purpose of this study the cloud is assumed to be isothermal, such that $B = B_0$. All quantities are monochromatic and cloud properties are considered to be uniform throughout. For illustrative purposes, a wavelength of 10μm is used in most of this work.

The two-stream approximation assumes that two quantities, I^+ and I^- represent the radiance and further that they are identified with the value of the radiance at $\mu = \pm\sqrt{\frac{1}{3}}$ which are the first-order gaussian quadrature points. Thus the scattering source function (3) may be written for the positive (upward) hemisphere as

$$\frac{\tilde{\omega}}{4\pi} \int_0^{2\pi} \int_{-1}^{1} I\,(x, y, z, \mu', \phi')\, p\left(\sqrt{\frac{1}{3}}, \phi; \mu', \phi'\right) d\mu'\, d\phi'$$

$$= \frac{\tilde{\omega}}{4\pi} \int_0^{2\pi} \left[I^+(x, y, z, \phi')\, p\left(\sqrt{\frac{1}{3}}, \phi; \sqrt{\frac{1}{3}}, \phi'\right) \right. \qquad (5)$$

$$\left. + I^-(x, y, z, \phi')\, p\left(\sqrt{\frac{1}{3}}, \phi; -\sqrt{\frac{1}{3}}, \phi'\right) \right] d\phi'$$

where I^+ is identified with $\mu = \sqrt{\frac{1}{3}}$ and I^- with $\mu = -\sqrt{\frac{1}{3}}$. If the phase function is expanded in a series consisting of the zero and first order Legendre functions, then

$$p\,(\mu, \phi; \mu', \phi') = 1 + 3g\,[\mu\mu' + \nu\nu' \cos(\phi - \phi')] \qquad (6)$$

where g is the asymmetry parameter. Substituting for μ and μ', the R.H.S. of (5) reduces to

$$\frac{\tilde{\omega}}{4\pi}\int_0^{2\pi} \left\{ I^+ [1 + g + 2g\cos(\phi - \phi')] + I^- [1 - g + 2g\cos(\phi - \phi')] \right\} d\phi'$$

Similarly for the downward hemisphere, we have

$$\frac{\tilde{\omega}}{4\pi}\int_0^{2\pi} \left\{ I^- [1 + g + 2g\cos(\phi - \phi')] + I^+ [1 - g + 2g\cos(\phi - \phi')] \right\} d\phi'$$

The equation of transfer in the vertical two-stream approximation follows from (2)

$$\begin{aligned} \sqrt{\frac{1}{3}}\frac{\partial I^+}{\partial z} + \sqrt{\frac{2}{3}}\cos\phi\,\frac{\partial I^+}{\partial x} + \sqrt{\frac{2}{3}}\sin\phi\,\frac{\partial I^+}{\partial y} &= -I^+ + (1 - \tilde{\omega})B_0 \\ &+ \frac{\tilde{\omega}}{4\pi}\int_0^{2\pi} \{ I^+ [1 + g + 2g\cos(\phi - \phi')] \\ &+ I^- [1 - g + 2g\cos(\phi - \phi')] \} d\phi' \end{aligned} \qquad (7a)$$

and

$$\begin{aligned} -\sqrt{\frac{1}{3}}\frac{\partial I^-}{\partial z} + \sqrt{\frac{2}{3}}\cos\phi\,\frac{\partial I^-}{\partial x} + \sqrt{\frac{2}{3}}\sin\phi\,\frac{\partial I^-}{\partial y} &= -I^- + (1 - \tilde{\omega})B_0 \\ &+ \frac{\tilde{\omega}}{4\pi}\int_0^{2\pi} \{ I^- [1 + g + 2g\cos(\phi - \phi')] \\ &+ I^+ [1 - g + 2g\cos(\phi - \phi')] \} d\phi' \end{aligned} \qquad (7b)$$

3. GOVERNING EQUATIONS AND BOUNDARY CONDITIONS

Eqs. (7a) and (7b) may be reduced by an expansion which employs the zero and first order Legendre functions:

$$I(x, y, z, \mu, \phi) = I'_c(x, y, z) + I'_z(x, y, z)\,\mu + I'_x(x, y, z)\,\nu\cos\phi + I'_y(x, y, z)\,\nu\sin\phi + \ldots.$$

In the two-stream approximation we will have

$$I^+(x, y, z, \phi) = I'_c + \sqrt{\frac{1}{3}}\,I'_z + \sqrt{\frac{2}{3}}\,I'_x\cos\phi + \sqrt{\frac{2}{3}}\,I'_y\sin\phi$$

and

$$I^-(x, y, z, \phi) = I'_c - \sqrt{\frac{1}{3}}\,I'_z + \sqrt{\frac{2}{3}}\,I'_x\cos\phi + \sqrt{\frac{2}{3}}\,I'_y\sin\phi$$

setting

$$I_z^{\pm} = I'_c \pm \sqrt{\frac{1}{3}}\,I'_z$$

$$I_x = \sqrt{\frac{2}{3}}\,I'_x$$

$$I_y = \sqrt{\frac{2}{3}}\,I'_y$$

yields

$$I^+ = I_z^+ + I_x\cos\phi + I_y\sin\phi \tag{8a}$$

and

$$I^- = I_z^- + I_x\cos\phi + I_y\sin\phi \tag{8b}$$

Further, letting

$$I_0 = \frac{1}{2}\left(I_z^+ + I_z^-\right)$$

and

$$I_1 = \frac{1}{2}\left(I_z^+ - I_z^-\right)$$

the scattering source function in (7a) and (7b) may be written as

$$\tilde{\omega} I_0 + \tilde{\omega} g I_1 + \tilde{\omega} g (I_x \cos\phi + I_y \sin\phi) \quad \text{positive hemisphere}$$

$$\tilde{\omega} I_0 - \tilde{\omega} g I_1 + \tilde{\omega} g (I_x \cos\phi + I_y \sin\phi) \quad \text{negative hemisphere}$$

Now, integration of Eqs. (7a) and (7b) by $\frac{1}{2\pi}\int_0^{2\pi} d\phi$ after substitution of (8a) and (8b) yields the following two equations

$$\sqrt{\frac{1}{3}}\frac{\partial I_z^+}{\partial z} + \sqrt{\frac{1}{6}}\left(\frac{\partial I_x}{\partial x} + \frac{\partial I_y}{\partial y}\right) = - I_z^+ + (1 - \tilde{\omega}) B_0 + \tilde{\omega} I_0 + \tilde{\omega} g I_1 \tag{9a}$$

and

$$-\sqrt{\frac{1}{3}}\frac{\partial I_z^-}{\partial z} + \sqrt{\frac{1}{6}}\left(\frac{\partial I_x}{\partial x} + \frac{\partial I_y}{\partial y}\right) = - I_z^- + (1 - \tilde{\omega}) B_0 + \tilde{\omega} I_0 - \tilde{\omega} g I_1 \tag{9b}$$

Adding (9a) and (9b) yields

$$\sqrt{\frac{1}{3}}\frac{\partial I_1}{\partial z} + \sqrt{\frac{1}{6}}\left(\frac{\partial I_x}{\partial x} + \frac{\partial I_y}{\partial y}\right) = - (1 - \tilde{\omega})(I_0 - B_0) \tag{10}$$

It can be shown that (10) satisfies the flux integral relation for this problem if first-order gaussian quadrature is used to evaluate integrals over μ. This equation is found in Chandrasekhar, (1960).

$$\nabla \cdot \underset{\sim}{F}_{net} = -4\pi (1 - \tilde{\omega})(I_0 - B_0) \tag{11}$$

where $\underset{\sim}{F}_{net}$ is the net flux vector. Subtracting (9b) from (9a) yields

$$\sqrt{\frac{1}{3}}\frac{\partial I_0}{\partial z} = -(1 - \tilde{\omega} g) I_1 \tag{12}$$

Integration of (7a) and (7b) by $\frac{1}{2\pi}\int_0^{2\pi} \cos\phi \, d\phi$ yields

$$\frac{1}{2}\sqrt{\frac{1}{3}}\frac{\partial I_x}{\partial z} + \frac{1}{2}\sqrt{\frac{2}{3}}\frac{\partial I_z^+}{\partial x} = -\frac{I_x}{2} + \tilde{\omega} g \frac{I_x}{2} \tag{13a}$$

and

$$-\frac{1}{2}\sqrt{\frac{1}{3}}\frac{\partial I_x}{\partial z} + \frac{1}{2}\sqrt{\frac{2}{3}}\frac{\partial I_z^-}{\partial x} = -\frac{I_x}{2} + \tilde{\omega} g \frac{I_x}{2} \tag{13b}$$

Adding (13a) and (13b) we have

$$\sqrt{\frac{2}{3}}\,\frac{\partial I_0}{\partial x} = -(1 - \tilde{\omega} g)\, I_x \tag{14}$$

Similarly it may be shown that

$$\sqrt{\frac{2}{3}}\,\frac{\partial I_0}{\partial y} = -(1 - \tilde{\omega} g)\, I_y \tag{15}$$

Combining (10), (11), (12), (14) and (15) yields

$$\nabla^2 I_0 = \lambda^2 (I_0 - B_0) \tag{16}$$

where

$$\lambda = [3(1 - \tilde{\omega})(1 - \tilde{\omega} g)]^{1/2}$$

is the inverse diffusion length. The boundary conditions for (16) are obtained from the flux conditions at the face of the cloud. Again, using the two-stream technique the fluxes may be written as

$$F_{z+,\,z+} = \int_0^{2\pi}\!\int_0^1 I^+ \mu \, d\mu \, d\phi = \pi (I_0 + I_1) = \pi \left(I_0 - \frac{1}{h'} \frac{\partial I_0}{\partial z} \right) \tag{17a}$$

$$F_{z-,\,z-} = \int_0^{2\pi}\!\int_{-1}^0 I^- \mu \, d\mu \, d\phi = -\pi (I_0 - I_1) = -\pi \left(I_0 + \frac{1}{h'} \frac{\partial I_0}{\partial z} \right) \tag{17b}$$

$$F_{x+,\,z+} = \int_{\frac{-\pi}{2}}^{\frac{\pi}{2}}\!\int_0^1 I^+ \nu \cos\phi \, d\mu \, d\phi = \frac{\pi}{2} \left(I_0 - I_1 + \frac{\pi}{4} I_x \right) \tag{17c}$$

$$F_{x+,\,z-} = \int_{\frac{-\pi}{2}}^{\frac{\pi}{2}}\!\int_{-1}^0 I^- \nu \cos\phi \, d\mu \, d\phi = \frac{\pi}{2} \left(I_0 + I_1 + \frac{\pi}{4} I_x \right) \tag{17d}$$

$$F_{x+,\,x+} = F_{x+,\,z+} + F_{x+,\,z-} = \pi \left(I_0 + \frac{\pi}{4} I_x \right) = \pi \left(I_0 - \frac{1}{h} \frac{\partial I_0}{\partial x} \right) \tag{17e}$$

Similarly

$$F_{x-,x-} = -\pi\left(I_0 + \frac{1}{h}\frac{\partial I_0}{\partial x}\right) \qquad (17f)$$

$$F_{y+,y+} = \pi\left(I_0 - \frac{1}{h}\frac{\partial I_0}{\partial y}\right) \qquad (17g)$$

$$F_{y-,y-} = -\pi\left(I_0 + \frac{1}{h}\frac{\partial I_0}{\partial y}\right) \qquad (17h)$$

Here, $h' = \sqrt{3}\,(1 - \tilde{\omega}g)$ and $h = \sqrt{\frac{3}{2}}\,\frac{4}{\pi}\,(1 - \tilde{\omega}g)$. Fluxes are illustrated in Figure 1 following Davies (1978). It is assumed that there is no flux incident at the top of the cloud and the bottom receives radiation only from the ground emitting at its black body temperature, T_1. The ground flux is πB_1 and the ground reflectivity is zero. The sides of the cuboidal cloud receive only the component of the flux emitted by the ground that is normal to the face. The use of flux boundary conditions leads to the loss of all directional information pertaining to the incoming radiation. This leads to slightly erroneous results for the radiance, a matter that is dealt with in Section 5 when Monte Carlo comparisons are made. Following the sign convention that flux is positive in the positive direction, the boundary conditions may now be written for a cloud of optical thickness z^* and equal sides, s. These are

$$\left(I_0 + \frac{1}{h'}\frac{\partial I_0}{\partial z}\right)_{z=z^*} = 0 \qquad (18a)$$

$$\left(I_0 - \frac{1}{h'}\frac{\partial I_0}{\partial z}\right)_{z=0} = B_1 \qquad (18b)$$

$$\left(I_0 + \frac{1}{h}\frac{\partial I_0}{\partial x}\right)_{x=s/2} = \frac{B_1}{2} \qquad (18c)$$

$$\left(I_0 - \frac{1}{h}\frac{\partial I_0}{\partial x}\right)_{x=-s/2} = \frac{B_1}{2} \qquad (18d)$$

$$\left(I_0 + \frac{1}{h}\frac{\partial I_0}{\partial y}\right)_{y=s/2} = \frac{B_1}{2} \tag{18e}$$

$$\left(I_0 - \frac{1}{h}\frac{\partial I_0}{\partial y}\right)_{y=-s/2} = \frac{B_1}{2} \tag{18f}$$

The above equations may be compared with similar equations in Weinman and Davies (1978) and Liou and Ou (1979). The difference lies in the parameters h and h′ in the above equations. In this form, the solution for horizontally finite clouds tends to the two-stream solution when the sides of the cloud are increased to infinity. It should be noted that although the x- and y-directions are interchangeable, that is not true of the vertical direction (note the difference between h and h′). This is a drawback as will be demonstrated later when numerical examples are presented but the errors are small. In our opinion, this is a modest price to pay for avoiding the unrealistic results obtained from the Eddington approximation.

4. MONTE CARLO SIMULATION

In order to test the accuracy of the two-stream approach, the transfer problem was also solved using a direct Monte Carlo simulation. The Monte Carlo model used is very similar to that described by Davies (1978) and Weinman and Davies (1978), and only the extensions needed for the current application are given here.

It is helpful to consider three separate sources of thermal photons: those emitted uniformly from within the cloud, those emitted from the ground immediately below the cloud base, and those emitted from the ground which strike the cloud sides. A summary of the simulation characteristics of each source type is presented in Table 1, which shows the energy per simulated photon as well as how the choice of initial coordinates and direction cosines for each photon is made.

As a result of the subsequent random walk of each photon, simulating the transfer of thermal radiation, a number of photons from each source type may ultimately exit the cloud surface through an area A in a solid angle bin at a mean angle θ to the normal to A. That is

$$\overline{\cos\theta} = \int_{\theta_1}^{\theta_2} \int_{\phi_1}^{\phi_2} \cos\theta \sin\theta \, d\theta \, d\phi \tag{19}$$

where $\theta_1, \theta_2, \phi_1, \phi_2$ mark the limits of the solid angle. If n_1 such photons have energy E_1 each, n_2 have E_2, and n_3 have E_3, the total simulated radiance through A in the direction defined by θ is then given by

$$I = (n_1 E_1 + n_2 E_2 + n_3 E_3)/A\,\overline{\cos\theta} \tag{20}$$

The stochastic nature of the Monte Carlo simulation causes its results to contain an element of uncertainty, which may be objectively assessed (Davies. 1978). We also note that the Monte Carlo solutions tend to the correct plane parallel solutions as $s/z \rightarrow \infty$.

As an additional check of the two-stream approximation, the source of photons incident on the cloud sides was altered in the so-called "modified Monte Carlo" version. For this version, the energy per unit area incident on the cloud sides was unchanged, but the initial direction cosines were chosen to be equally distributed in the upward and downward directions. This simulated the two-stream approximation more closely, but it no longer directly simulated the actual problem. In the next section, two-stream results will be compared with Monte Carlo simulations.

5. RESULTS

a. Fluxes

The solution of (16) subject to the boundary conditions (18) is obtained using finite Fourier transforms and is described in detail in Weinman and Davies (1978). We start by defining

$$\mathcal{I}(\zeta_i, \zeta_j, z) = \int_{-\frac{s}{2}}^{\frac{s}{2}} \int_{-\frac{s}{2}}^{\frac{s}{2}} \left[I_0\,(x, y, z) - \frac{B_1}{2} \right] \cos(\zeta_i x) \cos(\zeta_j y)\, dx\, dy \tag{21}$$

where ζ_i and ζ_j are eigenvalues to be defined later. All the quantities of interest may be derived from I_0 which is given by

$$I_0 = \sum_i \sum_j \frac{4\, \zeta_i\, \zeta_j \cos(\zeta_i x) \cos(\zeta_j y)\, \mathcal{I}(\zeta_i, \zeta_j, z)}{[\zeta_i s + \sin(\zeta_i s)]\, [\zeta_j s + \sin(\zeta_j s)]} + \frac{B_1}{2} \tag{22}$$

Here, ζ_i and ζ_j satisfy

$$\zeta_{i,\,j} = h \cot(\zeta_{i,\,j}\, s/2) \tag{23}$$

and

$$\mathcal{I} = C_+ e^{\Lambda z} + C_- e^{-\Lambda z} - (\chi/\Lambda^2) \tag{24}$$

where

$$\Lambda^2 = \lambda^2 + \zeta_i^2 + \zeta_j^2 \tag{25}$$

and

$$\chi = \frac{4\lambda^2}{\zeta_i \zeta_j} \left(\frac{B_1}{2} - B_0 \right) \sin\left(\frac{\zeta_i s}{2} \right) \sin\left(\frac{\zeta_j s}{2} \right) \tag{26}$$

The constants C_+ and C_- are determined from the transformed boundary conditions (18a) and (18b) which are

$$\left(\mathcal{I} + \frac{1}{h'} \frac{\partial \mathcal{I}}{\partial z} \right)_{z=z^*} = -\frac{2B_1}{\zeta_i \zeta_j} \sin\left(\frac{\zeta_i s}{2} \right) \sin\left(\frac{\zeta_j s}{2} \right) \tag{27a}$$

and

$$\left(\mathcal{I} - \frac{1}{h'} \frac{\partial \mathcal{I}}{\partial z} \right)_{z=0} = \frac{2B_1}{\zeta_i \zeta_j} \sin\left(\frac{\zeta_i s}{2} \right) \sin\left(\frac{\zeta_j s}{2} \right) \tag{27b}$$

To obtain the flux exiting each face of the cloud Eqs. (17a)–(17h) are evaluated at the appropriate face. The monochromatic emittance, transmittance and reflectance of plane parallel clouds have been used to identify their radiative behavior. Analogous definitions for horizontally finite clouds are not universally accepted and there is no general consensus available on these parameters. Here we define the emittance in terms of the flux exiting a particular face of the model cuboidal cloud. For an isolated, isothermal cloud at temperature T_0, the emittance of the top face is the ratio

$$(F_{z+,\,z+})_{z=z*}/\pi B_0$$

and the emittance of the side face at $x = \frac{s}{2}$ is

$$(F_{x+,\,x+})_{x=s/2}/\pi B_0$$

and so on for all the faces. Note that there is no ground contribution and $F_{z+,\,z+}$ is a function of x and y while $F_{x+,\,x+}$ is a function of y and z, unlike the plane parallel problem. Now if we consider the cloud at absolute zero over a black ground at temperature T_1, the reflectance of the bottom face of the cloud is defined as the ratio

$$(F_{z-,\,z-})_{z=0}/\pi B_1$$

The transmittance of the top face of the cloud is defined as the ratio

$$(F_{z+,\,z+})_{z=z*}/\pi B_1$$

and we have also defined the flux exiting the four faces as transmittance, i.e.

$$(F_{x+,\,x+})_{x=s/2}/\pi B_1$$

and so on. The advantage of these definitions is that they coincide with the plane parallel definitions when the sides of the cloud extend to infinity. Moreover, for a black ground the solutions for the cloud at absolute zero and ground at absolute zero can be superimposed to yield the radiative field. The present definitions are only a function of cloud characteristics, i.e., $\tilde{\omega}$, g, and optical dimensions z^* and s. They are thus independent of temperature and they differ from those presented by Liou and Ou (1979).

The point hemispheric flux exiting a cuboidal cloud of optical dimensions $(s, s, z^*) = (1, 1, 1)$ is shown schematically in Figure 2. Scattering parameters $\tilde{\omega} = 0.638$ and $g = 0.865$ are representative of a C-1 water cloud at 10μm (Deirmendjian, 1969). In the figures, H and L refer to relatively high and low flux and the contours indicate the flux pattern. The notable feature here is that emission is strongest from the interior regions of the cloud face whereas upward transmission is greater around the edges. The source of transmitted radiation is below the cloud so that relatively little radiation from below penetrates to the top and there is a gradient in the flux exiting the sides. The flux patterns for a superposition of an isothermal cloud on a black ground will be the Planck weighted addition of the emission and transmission results. Thus the composite case may show edge darkening or brightening of the top face depending on the optical dimensions, scattering properties and the temperatures of the cloud and ground.

The particular case of a cubic cloud of optical dimensions $(s, s, z^*) = (10, 10, 10)$ at 250K above a black ground at 300K is shown in Figures 3 and 4. Figure 3 gives the upward flux exiting the top face, $(F_{z+,\,z+})_{z=z^*}$, expressed in equivalent black body temperature for both the isolated (no ground) and composite configurations. The flux in the central portion of the cloud face at optical distances λ^{-1} (= 1.43 for this case) from the edge. is equal to the value obtained for plane parallel clouds. Figure 4 shows the upward component of the flux exiting each side of the cube, $(F_{x+,\,z+})_{x=s/2}$, which is given by (17c). Note that the effect of the underlying base can be seen in the composite case at the bottom edge. The figures show quite clearly that finite clouds cannot be considered black emitters when the radiative flux is computed.

A comparison of fluxes obtained with the Monte Carlo method is shown in Figure 5; the Monte Carlo results are shown in parenthesis. Values correspond to the average flux in the boxed area expressed in °K with the lead digit 2 suppressed for clarity. The boxes left unfilled may be completed using symmetry. The largest differences appear at the edges in the composite case (~ 10°K) and may be attributable to the fact that the diffusion approximation breaks down. An error is also introduced in the comparison over large bins where the flux varies rapidly. The RMS differences between the analytic results and Monte Carlo simulations are summarized in Table 2 in which the (10, 10, 2) case has also been included. It may be noted that use of the "modified Monte Carlo" reduces the RMS error for side fluxes considerably. This indicates that there is an inherent defect in the use of flux boundary conditions in Eqs. (18c)–(18f).

The flux patterns shown averaged over each face yield the mean hemispheric flux exiting each face. This quantity may then be used to perform a bulk radiative balance for the cloud as a whole. From Eqs. (17a)–(17h) the average fluxes may be written as

$$\left(\bar{F}_{z+,\,z+}\right)_{z=z^*} = \frac{\pi}{s^2}\int_{-\frac{s}{2}}^{\frac{s}{2}}\int_{-\frac{s}{2}}^{\frac{s}{2}}\left(I_0 - \frac{1}{h'}\frac{\partial I_0}{\partial z}\right)_{z=z^*} dx\,dy$$

for the top face,

$$\left(\bar{F}_{z-,\,z-}\right)_{z=0} = \frac{\pi}{s^2}\int_{-\frac{s}{2}}^{\frac{s}{2}}\int_{-\frac{s}{2}}^{\frac{s}{2}}\left(I_0 + \frac{1}{h'}\frac{\partial I_0}{\partial z}\right)_{z=0} dx\,dy$$

for the bottom face,

$$\left(\bar{F}_{x+,\,x+}\right)_{x=s/2} = \frac{\pi}{sz^*}\int_{0}^{z^*}\int_{-\frac{s}{2}}^{\frac{s}{2}}\left(I_0 - \frac{1}{h}\frac{\partial I_0}{\partial x}\right)_{x=s/2} dy\,dz$$

for one side face, and so on.

The results of the integration, using (22) are as follows

$$(\bar{F}_{z+,\,z+})_{z=z^*} = \pi\left\{\frac{B_1}{2} + \frac{1}{s^2}\sum_i\sum_j \frac{16\sin(\zeta_i s/2)\sin(\zeta_j s/2)}{[\zeta_i s + \sin(\zeta_i s)]\,[\zeta_j s + \sin(\zeta_j s)]} \times \left[\mathcal{I}(\zeta_i, \zeta_j, z^*) - \frac{1}{h'}\frac{\partial \mathcal{I}}{\partial z}(\zeta_i, \zeta_j, z^*)\right]\right\} \tag{28a}$$

$$(\bar{F}_{z-,\,z-})_{z=0} = \pi\left\{\frac{B_1}{2} + \frac{1}{s^2}\sum_i\sum_j \frac{16\sin(\zeta_i s/2)\sin(\zeta_j s/2)}{[\zeta_i s + \sin(\zeta_i s)]\,[\zeta_j s + \sin(\zeta_j s)]} \times \left[\mathcal{I}(\zeta_i, \zeta_j, 0) + \frac{1}{h'}\frac{\partial \mathcal{I}}{\partial z}(\zeta_i, \zeta_j, 0)\right]\right\} \tag{28b}$$

$$(\bar{F}_{x+,\,x+})_{x=s/2} = \pi\left\{\frac{B_1}{2} + \frac{1}{sz^*}\sum_i\sum_j \frac{16\,\zeta_i\cos(\zeta_i s/2)\sin(\zeta_j s/2)}{[\zeta_i s + \sin(\zeta_i s)]\,[\zeta_j s + \sin(\zeta_j s)]} \times \left[\frac{C_+}{\Lambda}(e^{\Lambda z^*} - 1) + \frac{C_-}{\Lambda}(1 - e^{-\Lambda z^*}) - \left(\frac{x}{\Lambda^2}\right)z^*\right]\right\} \tag{28c}$$

and so on.

Thus the mean emittance of the top face of an isothermal, isolated ($B_1 = 0$) cuboidal cloud is the ratio $(\bar{F}_{z+,z+})_{z=z^*}/\pi B_0$. This is plotted in Figure 6 for two finite cloud geometries, one cubic and one with horizontal dimensions ten times the vertical; the ordinate shows the vertical optical thickness, z*. Also plotted are plane parallel results obtained using the two-stream approximation and an accurate Neumann solution using the Henyey–Greenstein phase function.[1] The mean emittance of the top face of the cuboidal cloud falls short of that of plane parallel clouds of the same optical properties and depth. This differs from the results

---

[1] W. S. Olson (personal communication)

of the Eddington approximation shown in Figure 6 of Liou and Ou (1979) in which the (10τ, 10τ, τ) case shows emittance in excess of the plane parallel cloud. Figure 6 of the present paper shows that Eddington emittance is consistently larger than the exact results and that it exceeds unity when $z^* \gtrsim 5$. Thus the finite Eddington approximation will overestimate the emittance, while the two-stream is seen to be an underestimate, but the plane parallel results are very close to the exact for $z^* \sim 1$.

Although the top face of the model cloud emits less than the corresponding plane parallel cloud, the total emission from the cloud must include the contribution of the sides of the cloud. This is shown in the figure as the upward component of the side face emittance. For the cubic cloud, the contribution of the four side faces exceeds the emission from the top face and the total emission from the cloud is actually greater than the corresponding plane parallel cloud. The (10τ, 10τ, τ) case also shows total emittance greater than the plane parallel. If the cloud is not isolated, a portion of the side emission will be intercepted by neighboring clouds, thereby decreasing the total emittance.

b. Cooling Rates

The net flux divergence within the cloud gives the infrared cooling or heating experienced by each element of the cloud. For the three dimensional problem the cooling rate is given by

$$\frac{\partial T}{\partial t} = -\frac{1}{\rho C_p} \nabla \cdot \underset{\sim}{F}_{net} \tag{29}$$

where the net flux divergence is obtained from Eq. (11). Here ρ is the air density assumed to be $7.2 \times 10^{-4}\,g\,cm^{-3}$ and C_p the specific heat at constant pressure taken to be 1 J g^{-1} °C^{-1}. For illustration, we have computed spectral cooling rates in the 8–13.6 μm region. It was shown by Stephens (1978) that the window cooling rate forms the bulk of the total cooling rate for plane parallel clouds, so the results presented here may be considered representative of the total flux divergence. The cloud is cubic of dimensions 1 km on each side at a temperature of −10°C; the ground is at 15°C. It is further assumed that the cloud is type C-1 of droplet density 100 particles/cm^3 having optical properties tabulated in Deirmendjian (1969).

Figure 7 compares the horizontally averaged cooling rate of the cubic cloud with a plane parallel cloud of the same height. The additional cooling from the sides of the cloud increases the mean cooling at each level in the cloud. The level at which cooling to space is overcome by heating from the ground is lowered by 320m. What is even more striking is the distribution of net flux divergence at each level. Figure 8 shows the heating and cooling at four levels within the cloud marked A, B, C, D on Figure 7. The stippled areas indicate that heating is confined to the core at the 400 and 300 m levels, and cooling is around the edges. In regions close to the cloud base, such as level D, which is 100m above the base, the horizontally averaged divergence indicates heating as is evident from Figure 7 but Figure 8 shows that there is an outer skin that exhibits cooling.

The model illustrated here has a low droplet density. Additional computations have been performed for denser clouds and are presented in Table 3 which shows the horizontally averaged net flux divergence at selected levels within the cloud. Optically thicker clouds have more extreme divergence rates at the top and base, consistent with results obtained from the plane parallel model.

c. Radiances

Although diffusion approximations furnish respectable results for fluxes, the radiance field derived from such methods is totally inadequate. For example, the two-stream approximation assumes a uniform radiance in each hemisphere. However, the two-stream approximation can be used to compute the scattering source function, J_s, from which the radiance emerging from the cloud boundary can be computed by path integration (Weinman and Davies, 1978).

The radiance exiting a finite cuboidal cloud as seen by a sensor that measures the area average radiance at some viewing angle is shown schematically in Figure 9. It is assumed that the radiance for azimuthal angle, $\phi = 0$, will suffice for comparison with a real cloud of slightly irregular shape. Because it is impossible to represent the detailed features of a real cloud, one azimuth angle is as good as any other for the level of sophistication of the model. The radiance exiting at a point x_0, y_0, z_0, on the face of the cloud may be written as

$$I(x_0, y_0, z_0, \theta, 0) = B_1\, e^{-S^*(\theta)} + \int_{x_l(\theta)}^{x_u(\theta)} \left\{(1-\varpi)\, B_0 + J_s\, [x_0, y_0, z_0\, (x, \theta), \theta, 0]\right\} e^{-S(\theta)}\, \frac{dx}{\nu} \qquad (30)$$

where J_s is the scattering source function given by (3) and the slant optical path lengths $S(\theta)$ and $S^*(\theta)$, the limits of integration $x_u(\theta)$ and $x_l(\theta)$ and the functional dependence $z(x, \theta)$ which defines the slant path are tabulated in Weinman and Davies (1978) and will not be repeated here. Note that the sign convention in that paper is the reverse of that used in this study. Davies (1980) has shown that this method of computing exiting radiances is superior to that which a first order Eddington expansion provides.

It remains to define the scattering source function in the two stream approximation. Here we may use the complete phase function expansion from Chandrasekhar (1960) instead of (6).

$$p(\mu, \phi; \mu', \phi') = \sum_{l=0}^{\infty} \varpi_l \left\{P_l(\mu)\, P_l(\mu') + 2 \sum_{m=1}^{l} \frac{(l-m)!}{(l+m)!}\, P_l^m(\mu)\, P_l^m(\mu') \cos m\, (\phi - \phi')\right\} \qquad (31)$$

where ϖ_l are the coefficients in the phase function expansion and $P_l(\mu)$ and $P_l^m(\mu)$ are the Legendre functions. The scattering source function can then be written as

$$J_s = \frac{\varpi}{4\pi} \int_0^{2\pi} \left\{\int_0^1 I^+ (\mu', \phi')\, p(\mu, \phi; \mu', \phi')\, d\mu' + \int_{-1}^{0} I^- (\mu', \phi')\, p(\mu, \phi; \mu', \phi')\, d\mu'\right\} d\phi' \qquad (32)$$

Now substituting for $I^{\pm}$ from (8) and $p(\mu, \phi; \mu', \phi')$ from (31), Eq. (32) can be integrated analytically using relations available in Hobson (1955) and Gradshteyn and Ryzhik (1965). The result is

$$J_s = \varpi I_0 + \varpi I_1 \left\{\frac{\varpi_1 \mu}{2} + \sum_{l=1}^{\infty} \varpi_{2l+1}\, P_{2l+1}(\mu) \left[\frac{(-1)(-3)(-5)\ldots(-2l+1)}{(2l+2)(2l)(2l-2)\ldots 2}\right]\right\}$$

$$+ \frac{\varpi\pi}{8}\, \nu (I_x \cos\phi + I_y \sin\phi) \left\{\varpi_1 + \sum_{l=1}^{\infty} \varpi_{2l+1}\, \frac{d}{d\mu} P_{2l+1}(\mu)\, {}_3F_2 \left(\frac{2l+3}{2}, -l, \frac{3}{2}, 2, 2; 1\right)\right\} \qquad (33)$$

where

$$ {}_3F_2 = 1 + \frac{\Gamma(2)\,\Gamma(2)}{\Gamma\left(\frac{2l+3}{2}\right)\Gamma(-l)\,\Gamma\left(\frac{3}{2}\right)} \sum_{k=1}^{l} \frac{\Gamma\left(\frac{2l+3}{2}+k\right)\Gamma(-l+k)\,\Gamma\left(\frac{3}{2}+k\right)}{\Gamma(2+k)\,\Gamma(2+k)\,k!} $$

If we choose the Henyey-Greenstein phase function to represent p, then $\varpi_1 = 3g$ and $\varpi_{2l+1} = (4l+3)\,g^{2l+1}$ (van de Hulst, 1980). For zenith angles less than 70° the series can be approximated quite well by

$$ J_s \approx \varpi \left\{ I_0 + gI_1 + \frac{3g\pi}{8}\,\nu\,(I_x \cos\phi + I_y \sin\phi) \right\} \qquad (34) $$

which has been used with a slight modification by Weinman et al. (1981).

After substituting (33) into (30), the radiances obtained can be analytically averaged over the projected areas furnishing lengthy expressions for the desired quantity. An illustrative result is shown in Figure 10 in which the emergent radiance of an isolated cuboidal cloud is plotted against the zenith angle of the viewing sensor. The radiance values are normalized against the black body emission of the cloud, B_0. The case $z^* = 5$ is considered; individual curves are labeled with the horizontal optical thickness, s. The anisotropic nature of the emergent radiation is evident. The radiance is sharply reduced for finite clouds and there is a significant angular dependence. It may be noted that the curve for (5, 5, 5) is nearly symmetrical about $\theta = 45°$. This shows that the slight asymmetry alluded to in Section 3 is of little consequence numerically. Also marked on the figure are plane parallel solutions obtained by path integration of the Eddington source function and a 16-stream discrete ordinate solution.[2] The two-stream solution is satisfactory for all angles while the Eddington approximation yields poorer results except around 50°.

---

[2] M.-L. Wu (personal communication).

The above case considered an isolated cloud. The combined radiance profile of a cloud at 250°K overlying a black surface at 300°K is shown in Figure 11 for optical dimensions (10, 10, 2) and (10, 10, 10) compared with the plane parallel solutions. The contribution of the side faces to the radiance at large zenith angles is a prominent feature of the results. The local maximum is a function of the geometry of the cloud. It may be noted that even at $\theta = 0°$ the finite cubic cloud with $z^* = s = 10$ appears 3.5°K warmer then the plane parallel model suggests. This discrepancy can affect the determination of cloud top heights from the observed brightness temperature of small cloud elements. The solution here assumes that the ground is at a uniform temperature over a large distance compared to the cloud dimensions. It is also possible to solve problems where the ground temperature immediately below the cloud differs from the surroundings, (see Weinman et al., 1981).

Another observation from Figure 11 is that the two-stream approximation is good when the optical depth is large but that it fails to reproduce the radiance profile with $z^* = 2$ in the plane parallel case. This is not a serious handicap because clouds in the infrared window usually have optical thickness of ~10 or more.

The detailed radiance pattern as viewed at $\theta = 50°$, $\phi = 0°$ is shown in Figure 12 in units of brightness temperature for a cubic cloud of optical dimensions (10, 10, 10). The pattern is shown for both the isolated cloud at 250°K and for the cloud over a black ground at 300°K. The sharp gradient at the edges of the cloud are a feature of the results, although the bulk of the cloud is seen to exhibit a nearly uniform radiance. Figure 13 shows a comparison of the analytical results with Monte Carlo simulations (in parenthesis) for the same case. Again, the lead digit 2 has been suppressed for clarity. Errors are seen to be confined primarily to the edges where the Monte Carlo results indicate a sharper gradient than the analytical results. The overall comparison is summarized in Table 2.

The same model cloud when viewed from directly overhead at $\theta = 0°$ shows the radiance pattern in Figure 14. It may be noted that the central portion of the cloud is brighter in emission (isolated) whereas the composite cloud on black ground shows brightening about the edges. Comparisons with Monte Carlo simulations are presented in Table 2. For the radiance, as for flux, the "modified Monte Carlo" generally gives closer agreement with the analytical results, again highlighting the problem introduced by the side flux boundary conditions of Eqs. (18c)–(18f).

6. SUMMARY

The results presented here illustrate the differences between radiation from finite and plane parallel models of clouds. These are

(1) Finite clouds do not behave as black emitters if their horizontal extent is of the same order as their vertical dimensions unless the optical thickness is much greater than the diffusion length, λ^{-1}.

(2) There is a significant infrared cooling out of the sides of finite clouds.

(3) The brightness temperature measured from a finite cloud by a low resolution sensor is higher than the cloud top temperature.

(4) The radiance pattern across the face of a finite cloud shows sharp gradients near the edges.

The two-stream approximation used in the study was shown to be within a few degrees of the Monte Carlo simulations for radiance measurements indicating that this computationally rapid method may be advantageously used to model the radiative characteristics of finite clouds.

Acknowledgments

We wish to thank W. S. Olson, U. of Wisconsin, for emittance computations used in Figure 6, Dr. M.-L. Wu, NASA/GSFC for radiance computations used in Figures 10 and 11 and Brian Auvine, U. of Wisconsin, for assistance with the Monte Carlo programming. This research was supported by funding provided by ARO-D grant DRXRO-DRP-15227-GS and NASA grants NSG-5209 and NAG 5-101.

REFERENCES

Barkstrom, B. R. and R. F. Arduini, 1977: The effect of finite horizontal size of clouds upon the visual albedo of the earth. Radiation in the Atmosphere, H.-J. Bolle, Ed., Science Press, Princeton, 188-190.

Chandrasekhar, S., 1960: Radiative Transfer. Dover, New York, 393 pp.

Davies, R., 1978: The effect of finite geometry on the three-dimensional transfer of solar irradiance in clouds. J. Atmos. Sci., 35, 1712-1725.

________, 1980: Fast azimuthally dependent model of the reflection of solar radiation by plane-parallel clouds. App. Opt., 19, 250-255.

________, and J. A. Weinman, 1977: Results from two models of the three-dimensional transfer of solar radiation in finite clouds. Radiation in the Atmosphere, H.-J. Bolle, Ed., Science Press, Princeton, 225-227.

Deirmendjian, D., 1969: Electromagnetic Scattering on Spherical Polydispersions. Elsevier, New York, 290 pp.

Ellingson, R. G., and E. Kolczynski, 1980: Cumulus clouds and infrared heating of the atmosphere. Preprints of the International Radiation Symposium, Fort Collins, CO., 474-476.

Gradshteyn, I. S., and I. M. Ryzhik, 1965: Tables of Integrals, Series and Products. Academic Press, New York, 1086 pp.

Hobson, E. W., 1955: The Theory of Spherical and Ellipsoidal Harmonics. Chelsea Publishing, New York, 500 pp.

Liou, K.-N., and S. C. Ou, 1979: Infrared radiative transfer in finite cloud layers. J. Atmos. Sci., 36, 1985-1996.

Lyzenga, D. R., 1973: Note on the modified two-stream approximation of Sagan and Pollack. Icarus, 19, 240-243.

McKee, T. B., and S. K. Cox, 1974: Scattering of visible radiation by finite clouds. J. Atmos. Sci., 31, 1885-1892.

Stephens, G. L., 1978: Radiation profiles in extended water clouds. I: Theory. J. Atmos. Sci., 35, 2111-2122.

van de Hulst, H. C., 1980: Multiple Light Scattering. Tables, Formulas, and Applications. Vols. 1 and 2. Academic Press, New York, 739 pp.

Weinman, J. A., and R. Davies, 1978: Thermal microwave radiance from horizontally finite clouds of hydrometeors. J. Geophys. Res., 83, 3099-3107.

____________, Harshvardhan and W. S. Olson, 1981: Infrared radiation emerging from smoke produced by brush fires. App. Opt., 20, 199-206.

Table 1
Monte Carlo Simulation Characteristics

Energy Per Photon	Starting Position	Starting Direction Cosines
(a) Internal Source		
$4\pi(1-\tilde{\omega})\,B_0\,s^2z^*/N_{10}$	uniform within cloud volume	isotropic
(b) Source at Cloud Base		
$\pi B_1\,s^2/N_{20}$	uniform on cloud base	$v = R_1{}^{1/2}$ $h_1 = (1-v^2)^{1/2}\cos 2\pi R_2$ $h_2 = (1-v^2)^{1/2}\sin 2\pi R_2$
(c) Source at Cloud Sides		
$2\pi B_1\,sz^*/N_{30}$	uniform on cloud sides	$h_1 = R_1{}^{1/2}$ $h_2 = (1-h_1^2)^{1/2}\cos \pi R_2$ $v = (1-h_1^2)^{1/2}\sin \pi R_2$
(d) Modified (c)		
$2\pi B_1\,sz^*/N_{30}$	uniform on cloud sides	$h_1 = R_1{}^{1/2}$ $h_2 = (1-h_1^2)^{1/2}\cos 2\pi R_2$ $v = (1-h_1^2)^{1/2}\sin 2\pi R_2$

B_0 = Planck function at cloud temperature
B_1 = Planck function at ground temperature
R_1, R_2 are random numbers, uniform on (0, 1)
v is the vertical direction cosine, positive upwards: h_1, h_2 are the horizontal direction cosines
N_{10}, N_{20}, N_{30} are the total number of simulated photons for each source type

Table 2

Comparison Between Two-Stream and Monte Carlo Simulations

$T_0 = 250^\circ K$ $T_1 = 300^\circ K$

			RMS Difference in °K	
			(10, 10, 10)	(10, 10, 2)
Top	Upward Hemispheric Flux	isolated	0.7	0.7
		composite	5.8 (MC) 4.9 (MMC)	4.8 (MC) 3.8 (MMC)
	Radiance at $\theta = 50^\circ$ $\phi = 0^\circ$	isolated	2.3	1.9
		composite	4.5 (MC) 1.7 (MMC)	2.0 (MC) 2.3 (MMC)
	Radiance at $\theta = 0^\circ$	isolated	3.6	2.6
		composite	1.3 (MC) 3.8 (MMC)	3.4 (MC) 2.7 (MMC)
Side	Upward Hemispheric Flux	isolated	2.0	4.3
		composite	7.2 (MC) 3.6 (MMC)	5.7 (MC) 4.7 (MMC)
	Radiance at $\theta = 50^\circ$ $\phi = 0^\circ$	isolated	2.7	3.3
		composite	2.1 (MC) 1.2 (MMC)	2.1 (MC) 1.8 (MMC)

isolated – cloud alone

composite – cloud over black ground

(MC) – correct Monte Carlo version with side flux only from the bottom

(MMC) – modified Monte Carlo, with same boundary conditions as analytic model, i.e. distributed side flux

Table 3
Horizontally Averaged Heating (+) and Cooling (-)
Rates in °C/hr in the 8–13.6μm Region

Height From Base (m)	Droplet Density No./cm^3			
	100	200	300	400
1000	-5.3	-10.8	-16.2	-21.6
950	-3.0	-3.5	-3.1	-2.5
900	-1.8	-1.4	-0.9	-0.6
500	-0.4	-0.4	-0.4	-0.4
100	+0.5	+0.2	+0.1	+0.2
50	+1.2	+1.5	+1.2	+0.9
0	+2.6	+5.6	+8.6	+11.6

Cloud is type C1 with horizontal dimensions (1 km, 1 km, 1 km) $T_0 = -10°C; T_1 = 15°C$

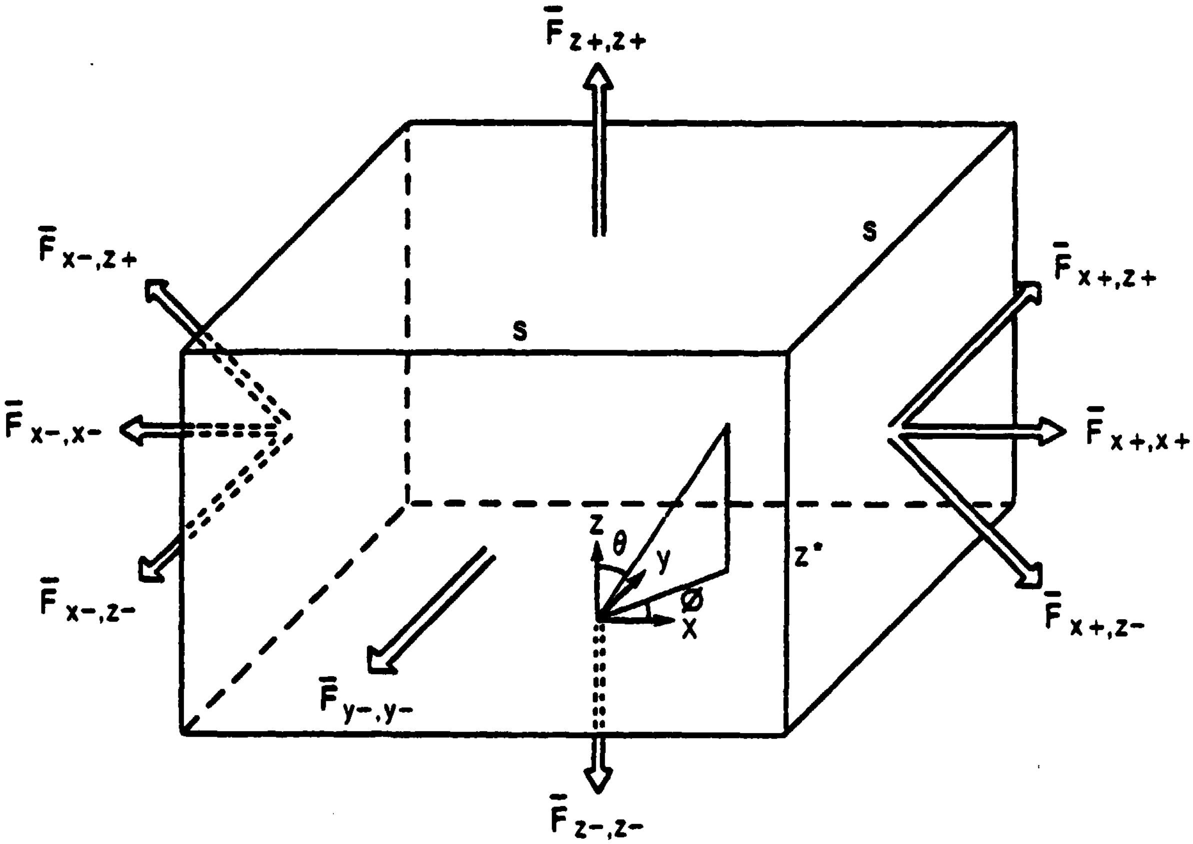

Fig. 1. Schematic illustration of coordinates and flux nomenclature.

ORIGINAL PAGE IS
OF POOR QUALITY

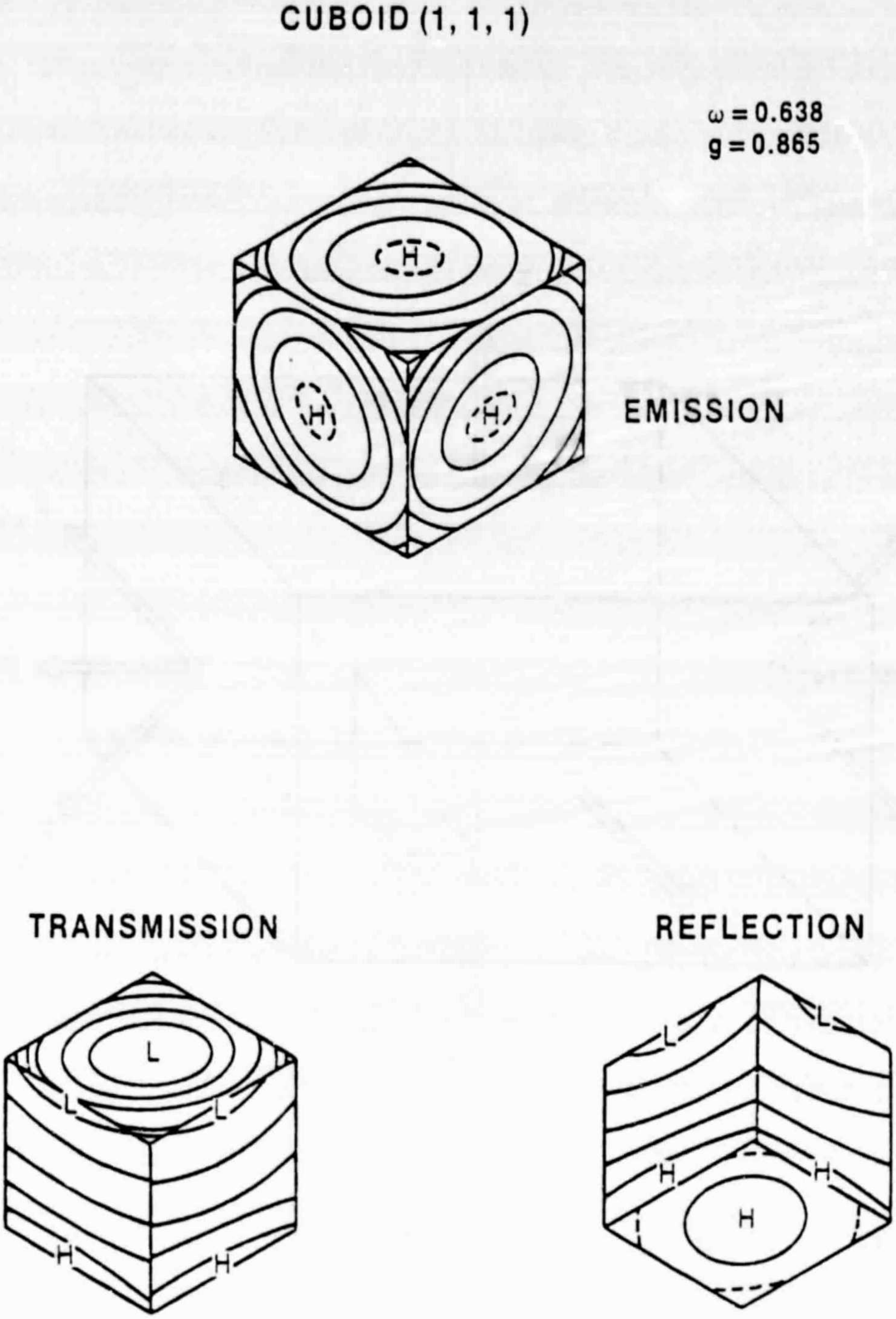

Fig. 2. Flux patterns on faces of cloud of optical dimensions (1, 1, 1).

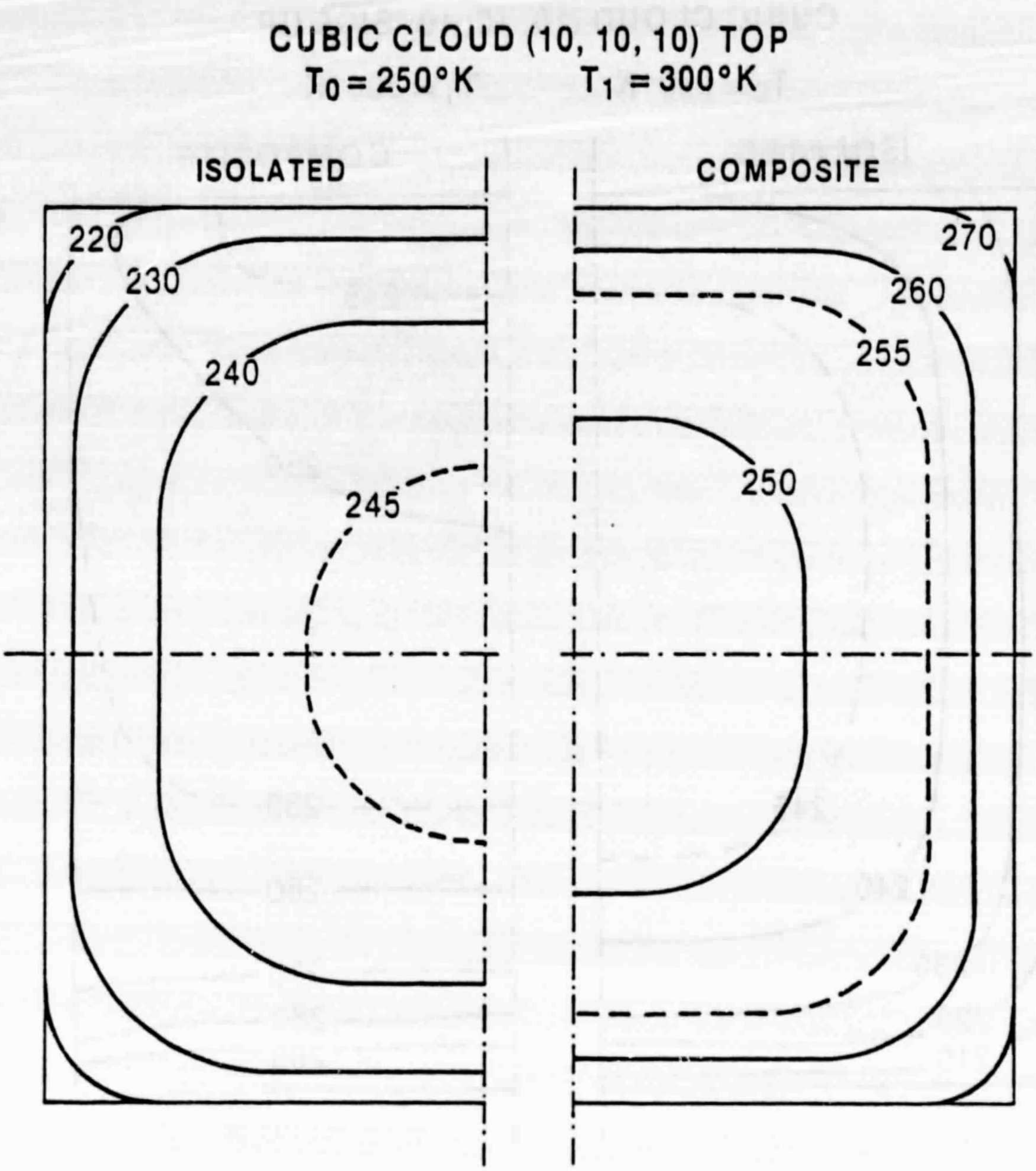

Fig. 3. Upward hemispheric flux, expressed as effective black body temperature, exiting the top face of a cubic cloud of optical dimensions (10, 10, 10). Isolated – cloud alone; composite – cloud over black ground.

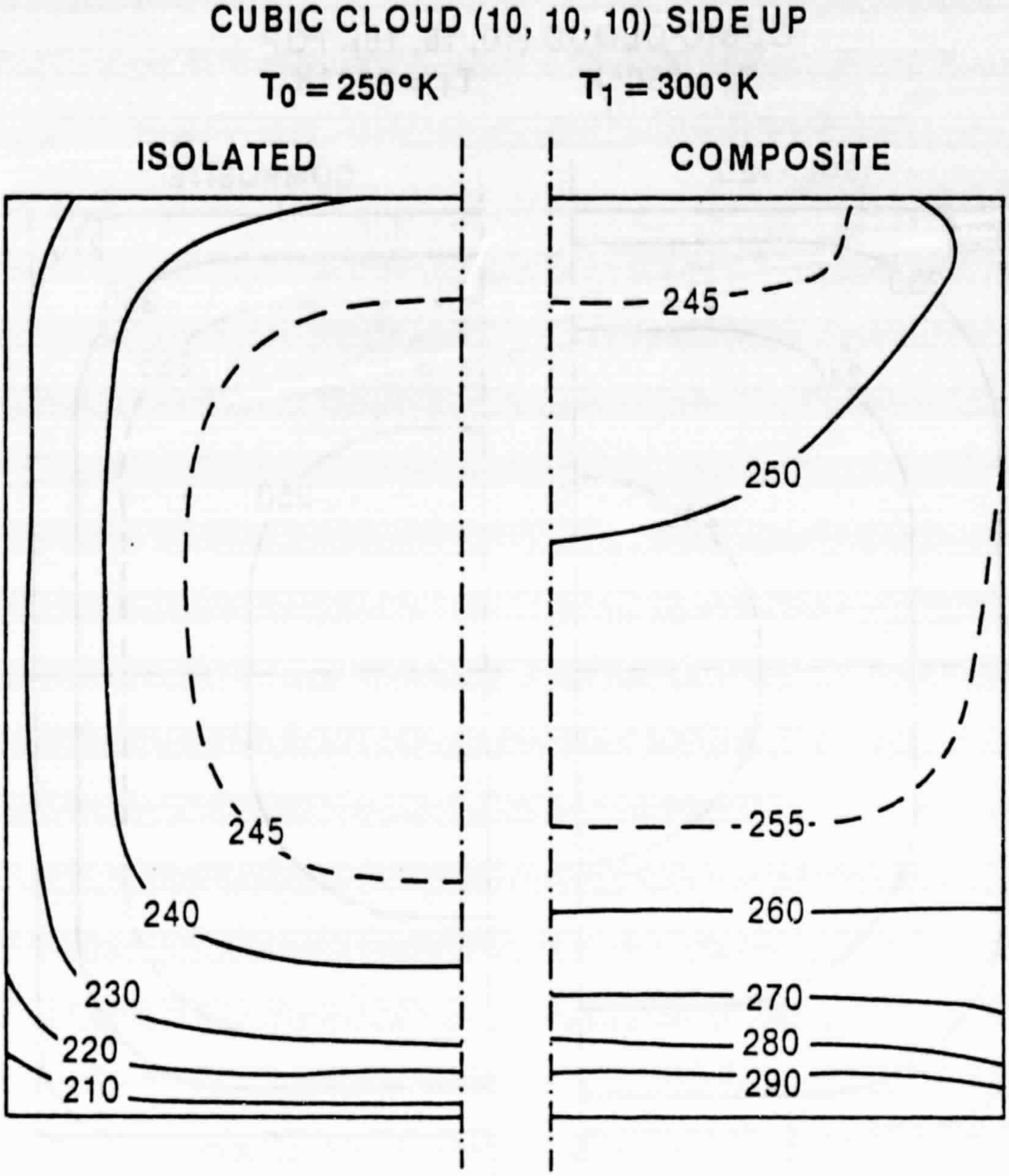

Fig. 4. Same as Figure 3, but upward component of hemispheric flux exiting each side face.

CUBIC CLOUD (10, 10, 10)
UPWARD HEMISPHERIC FLUX

$T_0 = 250°K$
$T_1 = 300°K$

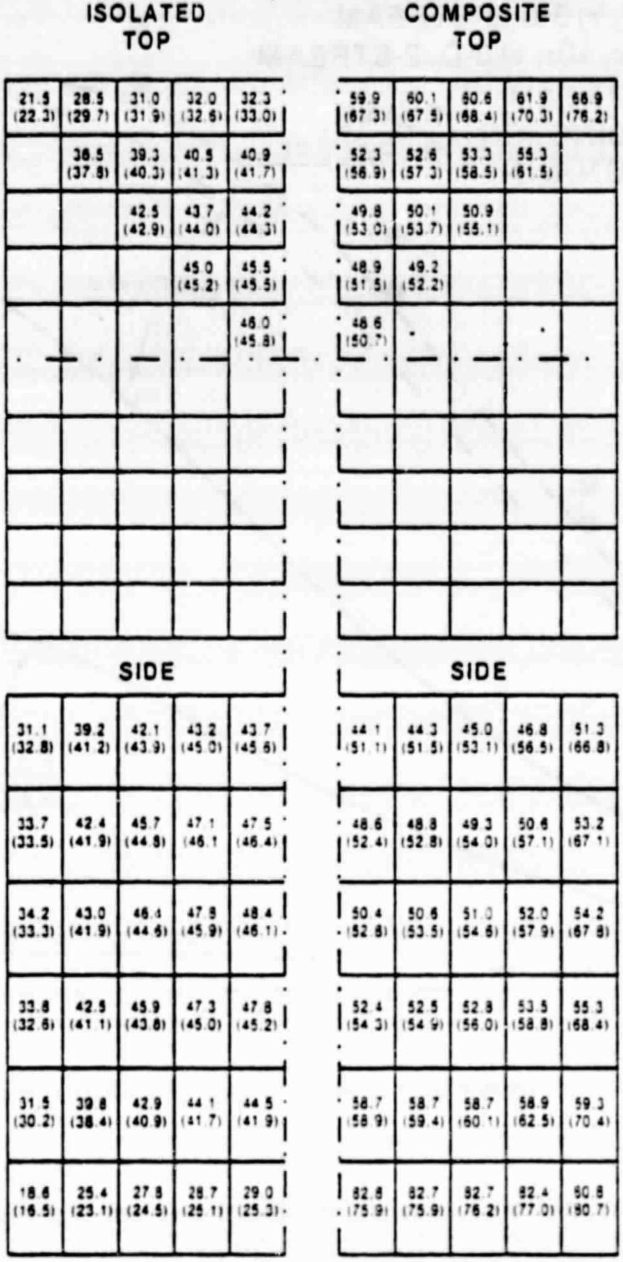

ISOLATED TOP

21.5 (22.3)	28.5 (29.7)	31.0 (31.9)	32.0 (32.6)	32.3 (33.0)
	38.5 (37.8)	39.3 (40.3)	40.5 (41.3)	40.9 (41.7)
		42.5 (42.9)	43.7 (44.0)	44.2 (44.3)
			45.0 (45.2)	45.5 (45.5)
				46.0 (45.8)

COMPOSITE TOP

59.9 (67.3)	60.1 (67.5)	60.6 (68.4)	61.9 (70.3)	68.9 (76.2)
52.3 (56.9)	52.6 (57.3)	53.3 (58.5)	55.3 (61.5)	
49.8 (53.0)	50.1 (53.7)	50.9 (55.1)		
48.9 (51.5)	49.2 (52.2)			
48.6 (50.7)				

ISOLATED SIDE

31.1 (32.8)	39.2 (41.2)	42.1 (43.9)	43.2 (45.0)	43.7 (45.6)
33.7 (33.5)	42.4 (41.9)	45.7 (44.8)	47.1 (46.1	47.5 (46.4)
34.2 (33.3)	43.0 (41.9)	46.4 (44.6)	47.8 (45.9)	48.4 (46.1)
33.8 (32.6)	42.5 (41.1)	45.9 (43.8)	47.3 (45.0)	47.8 (45.2)
31.5 (30.2)	39.8 (38.4)	42.9 (40.9)	44.1 (41.7)	44.5 (41.9)
18.6 (16.5)	25.4 (23.1)	27.8 (24.5)	28.7 (25.1)	29.0 (25.3)

COMPOSITE SIDE

44.1 (51.1)	44.3 (51.5)	45.0 (53.1)	46.8 (56.5)	51.3 (66.8)
48.6 (52.4)	48.8 (52.8)	49.3 (54.0)	50.6 (57.1)	53.2 (67.1)
50.4 (52.8)	50.6 (53.5)	51.0 (54.6)	52.0 (57.9)	54.2 (67.8)
52.4 (54.3)	52.5 (54.9)	52.8 (56.0)	53.5 (58.8)	55.3 (68.4)
58.7 (58.9)	58.7 (59.4)	58.7 (60.1)	58.9 (62.5)	59.3 (70.4)
82.8 (75.9)	82.7 (75.9)	82.7 (76.2)	82.4 (77.0)	90.8 (90.7)

Fig. 5. Comparison between two-stream and Monte Carlo simulations (in parenthesis) for cases given in Figures 3 and 4. Flux is expressed in effective black body temperature with the lead digit 2 suppressed for clarity. Empty boxes may be filled by symmetry.

ORIGINAL PAGE IS
OF POOR QUALITY

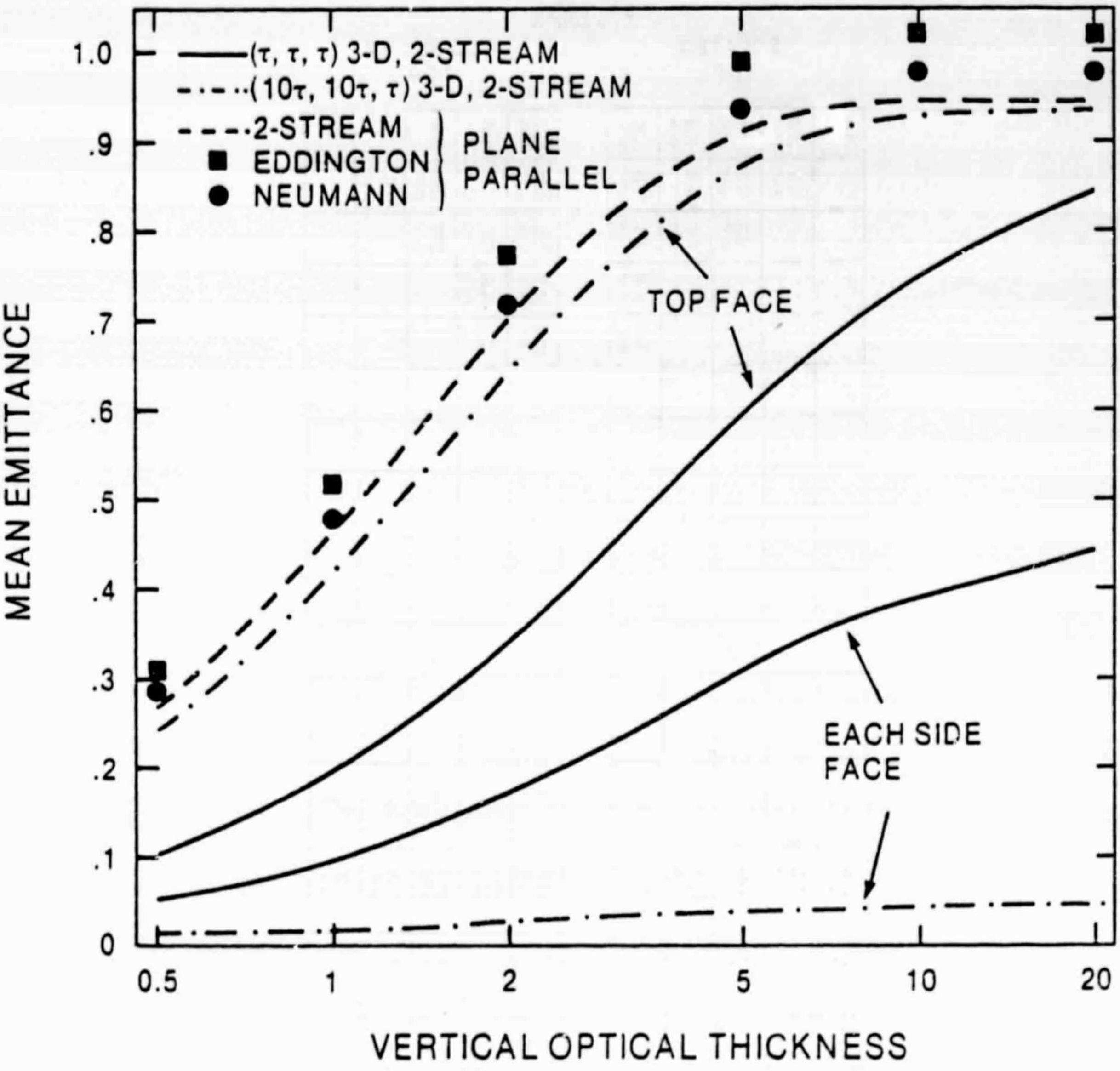

Fig. 6. Mean emittance of cloud faces. Henyey–Greenstein phase function has been used for the Neumann solution.

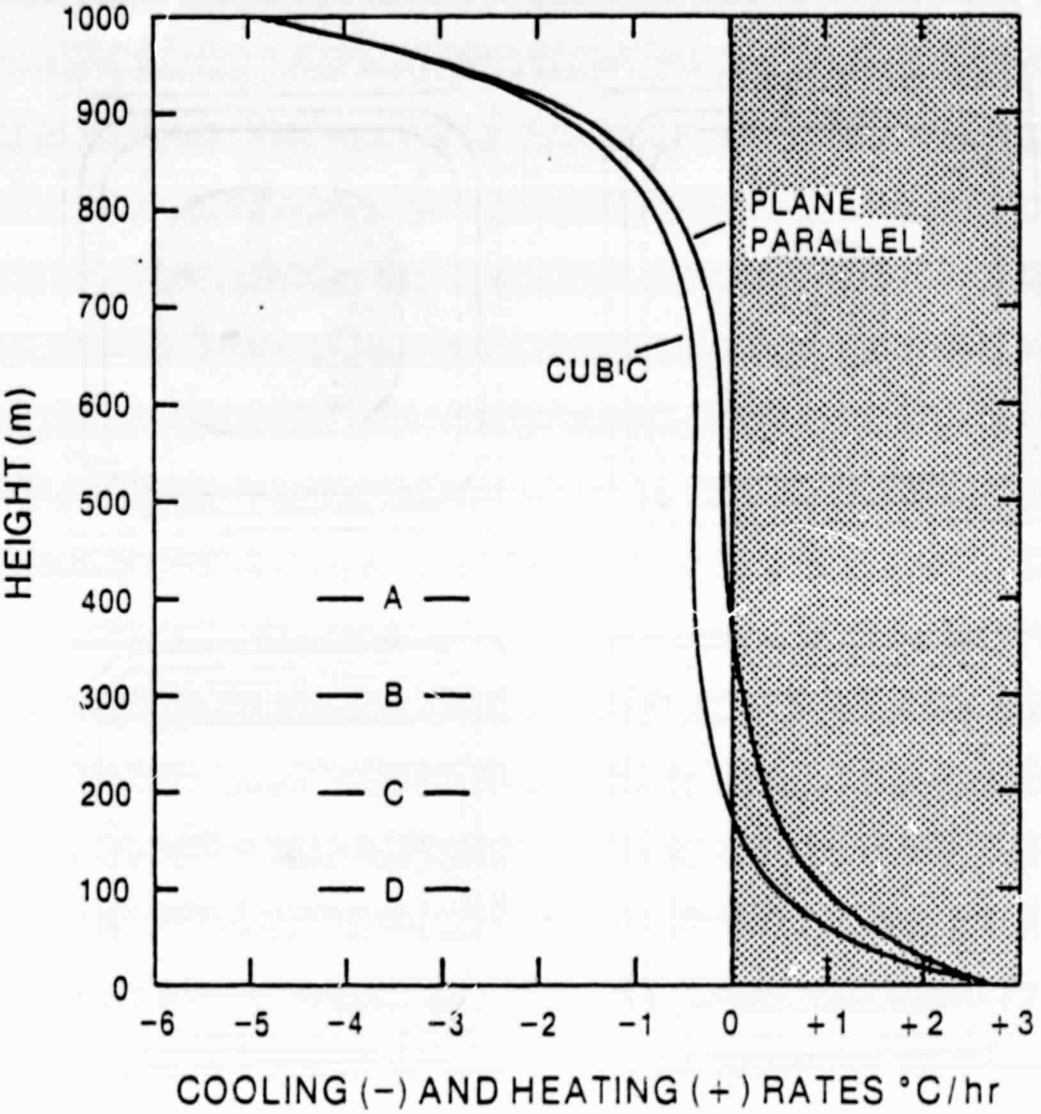

Fig. 7. Horizontally averaged heating (+) and cooling (−) rates in the 8–13.6 μm region within a 1 km cloud at −10° C overlying a black surface at 15° C. The cloud is type C-1 and has 100 particles/cm^3. Stippled areas show heating.

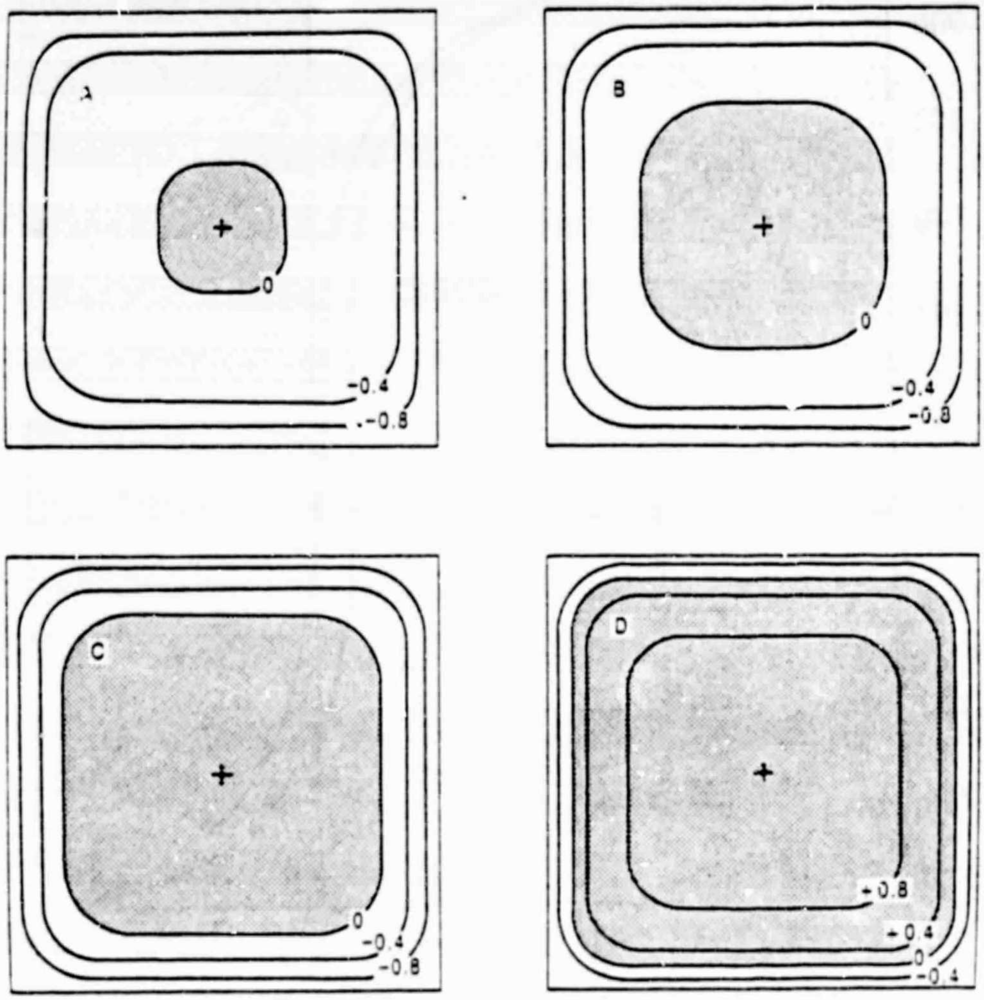

Fig. 8. Horizontal section at 400m (A), 300m (B), 200m (C) and 100m (D) above the base of the cloud showing the heating (+) and cooling (-) rate distribution in C/hr at each level.

ORIGINAL PAGE IS
OF POOR QUALITY

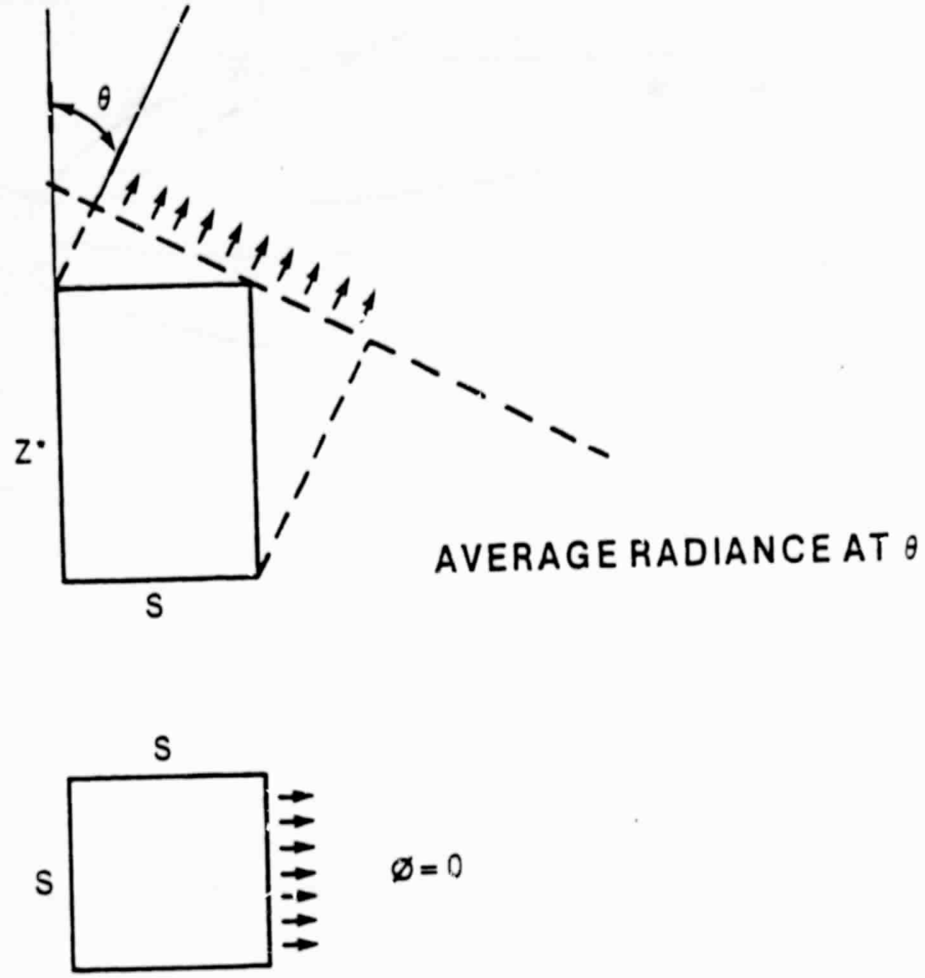

Fig. 9. Viewing geometry for sensing average radiance from cuboidal clouds.

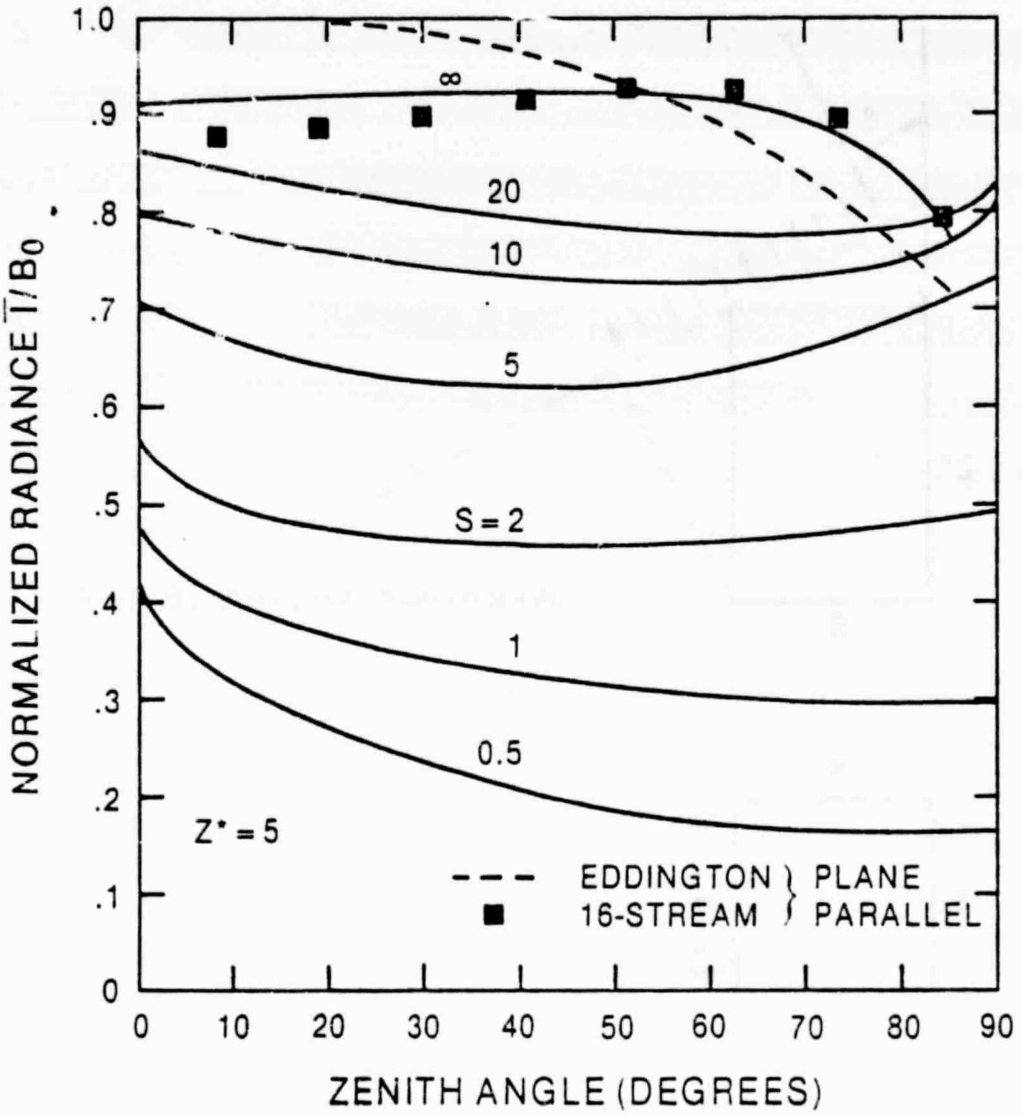

Fig. 10. Average normalized radiance as a function of zenith angle for an isolated cloud of optical depth, z*=5. Individual curves are marked with the horizontal optical thickness, s. Also shown are plane parallel results using the Eddington approximation and the sixteen-stream solution for which the Henyey–Greenstein phase function was used.

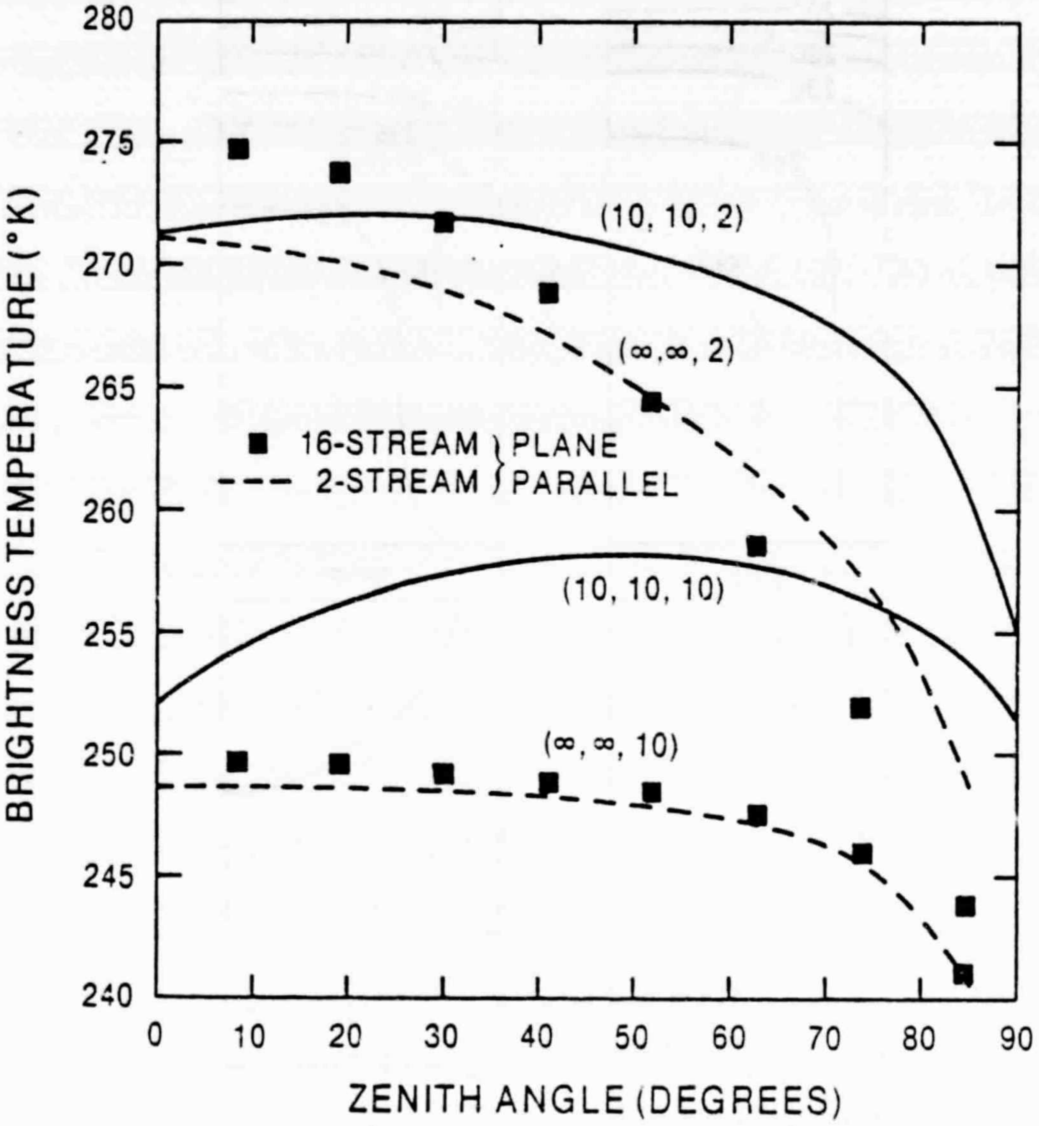

Fig. 11. Average radiance expressed as the brightness temperature as a function of zenith angle for clouds of optical dimension (10, 10, 2) and (10, 10, 10) compared with corresponding plane parallel clouds. $T_0 = 250°$ K, $T_1 = 300°$ K.

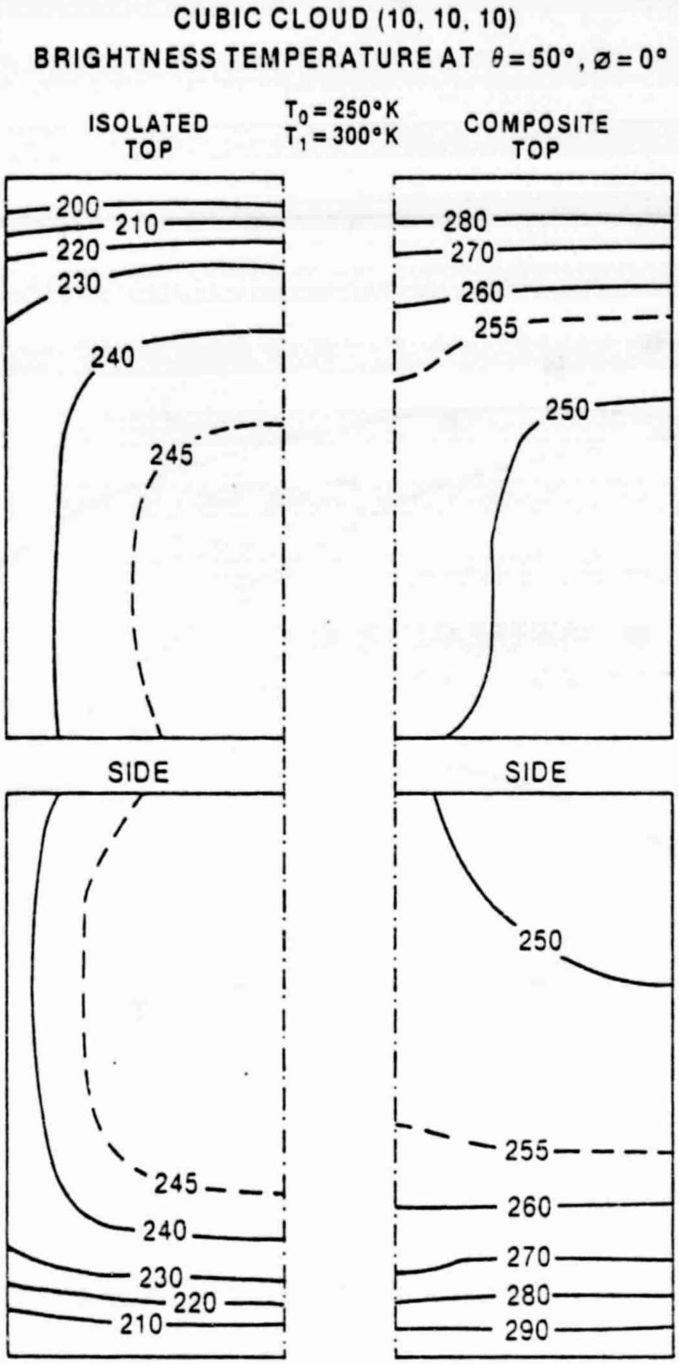

Fig. 12. Brightness temperature pattern of cloud of optical dimensions (10, 10, 10) at $\theta = 50°$, $\phi = 0°$.

CUBIC CLOUD (10, 10, 10)
BRIGHTNESS TEMPERATURE AT
$\theta = 50°$, $Ø = 0°$
$T_0 = 250°K$
$T_1 = 300°K$

ISOLATED
TOP

13.0 (13.2)	15.7 (12.8)	16.6 (14.7)	17.0 (14.5)	17.1 (14.4)
34.0 (38.1)	38.4 (38.9)	40.1 (39.8)	40.8 (39.7)	41.1 (39.7)
37.5 (42.5)	42.5 (44.4)	44.5 (45.1)	45.4 (44.8)	45.7 (45.7)
38.1 (42.8)	43.2 (45.4)	45.4 (46.6)	46.3 (46.1)	46.6 (46.7)
38.0 (42.3)	43.1 (46.0)	45.1 (46.2)	46.0 (47.4)	46.3 (47.4)

SIDE

39.2 (43.2)	44.5 (45.6)	46.6 (47.8)	47.5 (47.4)	47.9 (47.2)
40.2 (42.9)	45.7 (45.5)	48.1 (46.1)	49.1 (48.2)	49.5 (47.7)
39.9 (43.0)	45.4 (45.1)	47.7 (46.1)	48.7 (47.1)	49.0 (46.4)
37.2 (38.3)	42.1 (40.9)	44.1 (40.6)	45.0 (42.4)	45.3 (42.3)
17.9 (15.9)	21.1 (17.6)	22.3 (17.6)	22.8 (17.2)	23.0 (17.6)

COMPOSITE
TOP

75.6 (84.6)	75.7 (80.8)	75.8 (81.7)	76.1 (82.7)	76.8 (85.9)
52.7 (59.8)	52.8 (58.9)	53.2 (60.1)	54.2 (60.0)	56.5 (61.3)
48.9 (52.3)	49.0 (51.7)	49.6 (51.9)	50.8 (52.3)	53.7 (55.0)
48.3 (49.1)	48.5 (48.7)	49.0 (50.3)	50.4 (51.2)	53.4 (53.3)
47.8 (49.4)	48.0 (49.8)	48.5 (49.2)	49.8 (51.8)	52.9 (53.9)

SIDE

47.5 (50.1)	47.6 (50.7)	48.1 (51.7)	49.1 (52.1)	51.4 (54.1)
49.8 (51.9)	49.9 (52.2)	50.2 (51.4)	51.0 (52.6)	52.6 (55.1)
51.7 (52.7)	51.8 (53.4)	52.0 (53.6)	52.5 (54.0)	53.7 (57.2)
58.4 (59.6)	58.4 (59.3)	58.4 (58.4)	58.5 (60.2)	58.6 (60.9)
81.5 (80.1)	81.6 (80.1)	81.5 (79.2)	81.4 (82.0)	80.7 (82.3)

Fig. 13. Brightness temperature comparison between two-stream and Monte Carlo simulations (in parenthesis) for case shown in Figure 12. Lead digit 2 suppressed for clarity.

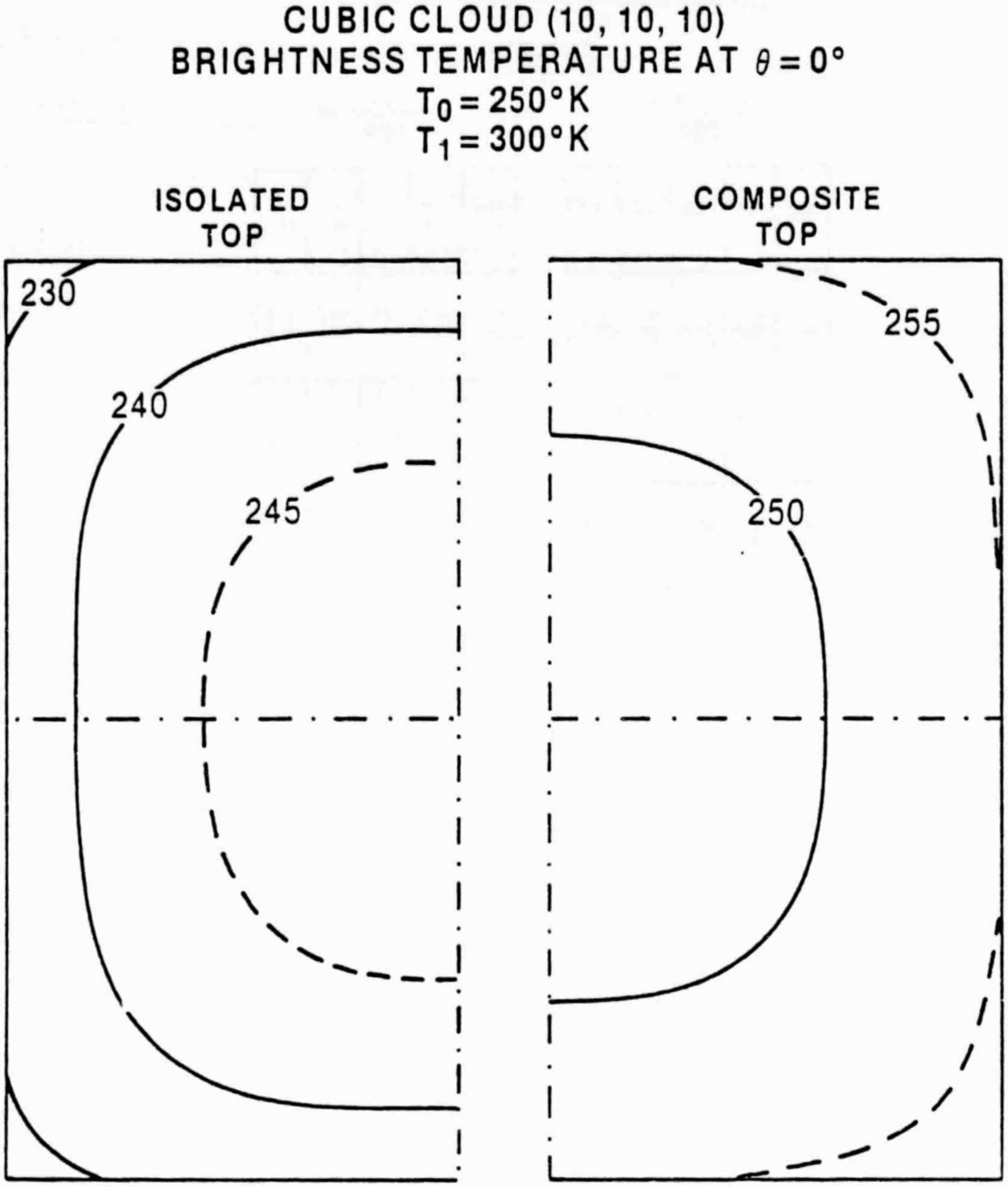

Fig. 14. Same as Fig. 12 but at θ = 0°.

BIBLIOGRAPHIC DATA SHEET

1. Report No. TM 82116	2. Government Accession No.	3. Recipient's Catalog No.
4. Title and Subtitle Transport of Infrared Radiation in Cuboidal Clouds		5. Report Date
		6. Performing Organization Code
7. Author(s) Harshvardhan, J. A. Weinman and R. Davies		8. Performing Organization Report No.
9. Performing Organization Name and Address National Aeronautics and Space Administration Goddard Space Flight Center Greenbelt, Md 20771		10. Work Unit No.
		11. Contract or Grant No. NSG-5209 and NAG 5-101
		13. Type of Report and Period Covered Technical Memorandum
12. Sponsoring Agency Name and Address		14. Sponsoring Agency Code
15. Supplementary Notes		

16. Abstract

The transport of infrared radiation in a single cuboidal cloud has been modeled using a vertical two-stream approximation. Computations have been made at 10 μm for a Deirmendjian (1969) C-1 water cloud of single scattering albedo, $\tilde{\omega} = 0.638$ and asymmetry parameter, $g = 0.865$. Results indicate that the emittance of the top face of the model cloud is always less than that for a plane parallel cloud of the same optical depth. The hemispheric flux escaping from the cloud top has a gradient from the center to the edges which brighten when the cloud is over warmer ground. Cooling rate calculations in the 8-13.6μm region show that there is cooling out of the sides of the cloud at all levels even when there is heating of the core from the ground below.

The radiances exiting from model cuboidal clouds were computed by path integration over the source function obtained with the two-stream approximation. Results suggest that the brightness temperature measured from finite clouds will overestimate the cloud top temperature.

Some key results of the model have been compared with Monte Carlo simulations. Overall errors in flux and radiance average a few degrees for most cases.

17. Key Words (Selected by Author(s)) Infrared Radiative Transport, Finite Clouds, Remote Sensing		18. Distribution Statement	
19. Security Classif. (of this report) Unclassified	20. Security Classif. (of this page) Unclassified	21. No. of Pages 28	22. Price*

*For sale by the National Technical Information Service, Springfield, Virginia 22151.